

Predicting areas of sustainable error growth in quasigeostrophic flows using perturbation alignment properties

By G. RIVIÈRE^{1,*} and B. L. HUA², ¹*Laboratoire de Météorologie Dynamique, Ecole Normale Supérieure, 75231 Paris Cedex 05, France;* ²*Laboratoire de Physique des Océans, IFREMER, BP 70, 29280 Plouzané, France*

(Manuscript received 25 April 2003; in final form 20 April 2004)

ABSTRACT

A new perturbation initialization method is used to quantify error growth due to inaccuracies of the forecast model initial conditions in a quasigeostrophic box ocean model describing a wind-driven double gyre circulation. This method is based on recent analytical results on Lagrangian alignment dynamics of the perturbation velocity vector in quasigeostrophic flows. More specifically, it consists in initializing a unique perturbation from the sole knowledge of the control flow properties at the initial time of the forecast and whose velocity vector orientation satisfies a Lagrangian equilibrium criterion. This Alignment-based Initialization method is hereafter denoted as the AI method.

In terms of spatial distribution of the errors, we have compared favorably the AI error forecast with the mean error obtained with a Monte-Carlo ensemble prediction. It is shown that the AI forecast is on average as efficient as the error forecast initialized with the leading singular vector for the palenstrophy norm, and significantly more efficient than that for total energy and enstrophy norms. Furthermore, a more precise examination shows that the AI forecast is systematically relevant for all control flows whereas the palenstrophy singular vector forecast leads sometimes to very good scores and sometimes to very bad ones.

A principal component analysis at the final time of the forecast shows that the AI mode spatial structure is comparable to that of the first eigenvector of the error covariance matrix for a “bred mode” ensemble. Furthermore, the kinetic energy of the AI mode grows at the same constant rate as that of the “bred modes” from the initial time to the final time of the forecast and is therefore characterized by a sustained phase of error growth. In this sense, the AI mode based on Lagrangian dynamics of the perturbation velocity orientation provides a rationale of the “bred mode” behavior.

1. Introduction

One major source of numerical error forecast in meteorology and oceanography comes from inaccuracies in initial conditions. The divergence of trajectories of models with initially close states is well-known since the pioneering works of Thompson (1957) and Lorenz (1965) in a meteorological context. In order to quantify error growth after a finite time T different strategies have been proposed. Leith (1974) used a Monte-Carlo approach (MC method hereafter): a large ensemble of N random perturbations is generated and added to an initial state to construct an ensemble of N nearby initial conditions, each member of the ensemble being the initial state of a simulation which is integrated for a finite time T . The result of each simulation after T can be considered

as a possible state and can be used to diagnose the average error growth. The MC method is computationally expensive because the number N of needed perturbations is apriori of the order of the number of degrees of freedom of the system and is thus not possible for an operational numerical weather prediction (NWP) model.

We can reduce the size of the ensemble by generating perturbations which are dynamically relevant instead of random. This is what is presently used in different operational NWP centers and two ensemble strategies are well-known (Ensemble Prediction Methods): at the European Centre for Medium-Range Weather Forecast (ECMWF) the ensemble is composed of perturbations that will grow most rapidly for the energy norm, this is the Singular Vector method (Buizza and Palmer, 1995; Molteni et al., 1996); at the National Center for Environmental Prediction (NCEP), the perturbations are created by the so-called breeding technique (Toth and Kalnay, 1993, 1997) and represent structures that have grown most rapidly in the past. At the Canadian Meteorological Centre, another strategy based on assimilation cycles

*Corresponding author.

e-mail: griviere@princeton.edu

¹present affiliation: GFDL Princeton University, Forrestal Campus, PO Box 308, NJ 08542 Princeton, USA

is used which is called the Perturbed Observation Method and consists in randomly sampling from the probability distribution of analysis errors (Houtekamer and Derome, 1995; Houtekamer et al., 1996; Hamill et al., 2000). Legras and Vautard (1996) show that the singular modes and the bred modes are related respectively to the forward Lyapunov modes and the backward Lyapunov modes. Even if they are not used as ensemble members in operational centers, the (backward) Lyapunov modes can have the same properties as the mean error growth determined by a Monte-Carlo approach as Vannitsem and Nicolis (1997) have shown in a quasi-geostrophic model. Other types of perturbations can be dynamically significant like the finite-time normal modes (eigenvectors of the tangent linear resolvent): for long time periods they resemble singular modes that have evolved; or the adjoint finite-time normal modes (eigenvectors of the adjoint of the tangent linear resolvent): for long optimization time periods they resemble singular modes (see Frederiksen, 1997, 2000). In an oceanographical context, research on predictability problems and error growth has not been as intensive but recently Moore (1999) studied in a model of the Gulf Stream the dynamics of error growth with ensemble forecasts and showed that singular modes and perturbations related to adjoint finite-time normal modes are more efficient for perturbing ensemble members.

Present approaches in operational centers are thus based on ensemble prediction. A recent paper from Patil et al. (2001) shows that, in global atmospheric models, few “bred modes” are necessary to represent the chaotic behavior of the atmosphere, and thus the number of ensemble members needed is much smaller than expected. More specifically, they define, at each point of the globe, a subspace from the local structures of the “bred modes” around this point. The authors found that in most regions, the “bred mode” subspace dimension is low. Similar results are presented in the recent works of Snyder and Hamill (2003) and Snyder et al. (2003). In these papers, it is shown that the spatial structures of initially random perturbations that have evolved on a time scale of $O(1 \text{ day})$ are comparable to the Lyapunov vectors structures and they are constrained in terms of both spatial scale and location by the unperturbed flow properties; in particular, their potential vorticity (PV) are concentrated where the gradient of the unperturbed flow PV is large. The above results are compatible with those found by Rivière et al. (2003) (referred to as RHK in the following) on alignment properties of perturbations that have grown in the past. In the latter paper, it is shown in a barotropic quasigeostrophic context, that the streamfunction isolines directions for initially random perturbations that have evolved for a finite time, converge at each spatial location toward a most probable direction. The most probable direction is deduced from an analytical analysis of the Lagrangian equilibria of the perturbation velocity vector orientation and can be analytically diagnosed from the knowledge of the reference unperturbed flow structure. Perturbations that have grown in the past (e.g. bred modes, Lyapunov vectors or initially random perturbations that have evolved for a finite time) are not only constrained in terms of spatial scale and energy by the control flow but also

in terms of alignment properties. The first objective of the paper is to relate more closely the notion of sustainable error growth characteristic of the perturbations that have grown in the past to the most probable direction determined in RHK.

The second objective is to test a new perturbation initialization method for quantifying error growth in quasigeostrophic flows. It consists in initializing a unique perturbation having the closest alignment with the most probable direction at each spatial location and in verifying that its evolution characterizes the statistical behavior of error growth. This Alignment-based initialization method is hereafter denoted as the AI method. In other words, is the initial alignment of the perturbation an essential ingredient for sustainable error growth? In order to test the statistical relevance of this unique perturbation, error growth deduced from its time evolution will be compared with error growth computed from classical methods (Monte-Carlo, singular vectors and bred vectors methods).

The present paper is organized as follows: Section 2 recalls briefly analytical results deduced from the linearized momentum equations that allow us to define the most probable structure; the quasigeostrophic ocean model, the initialization algorithm for the perturbation with the most probable structure as well as the classical numerical methods (Monte-Carlo, singular vectors and bred vectors methods) are described in Section 3; Section 4 is devoted to the numerical results and in particular the different error forecasts and their intercomparison in terms of spatial localization; and Section 5 provides a discussion of our results.

2. Lagrangian dynamics of the perturbation velocity

2.1. Barotropic perturbation kinetic energy equation

Our approach for diagnosing initial error growth consists in studying the dynamics of spatially localized interactions that allow a perturbation to extract kinetic energy from the unperturbed control flow. In a barotropic context, these local interactions can be studied from the perturbation kinetic energy equation, obtained from the linearized version of the momentum equations

$$\frac{\bar{D}K'}{Dt} = \bar{E} \cdot \bar{D} - \bar{u}' \cdot \bar{\nabla} p'_1. \quad (1)$$

The notations used in the previous equation follow the formalism of Mak and Cai (1989) who have analyzed the different terms of the equation; bars denote quantities associated with the control flow, while primes denote perturbations, \bar{u} is the geostrophic velocity field, $K' \equiv \frac{1}{2}|\bar{u}'|^2$ is the perturbation kinetic energy, p_1 is the ageostrophic pressure and let us emphasize that $\frac{D}{Dt} \equiv \partial/\partial t + (\bar{u} \cdot \bar{\nabla})$ is the control flow Lagrangian derivative and that our framework is intrinsically Lagrangian. Furthermore, the vectors \bar{E} and \bar{D} are defined by

$$\begin{aligned} \bar{E} &\equiv \left\{ \frac{1}{2}(v'^2 - u'^2), -u'v' \right\}, \\ \bar{D} &\equiv (\partial_x \bar{u} - \partial_y \bar{v}, \partial_x \bar{v} + \partial_y \bar{u}), \end{aligned} \quad (2)$$

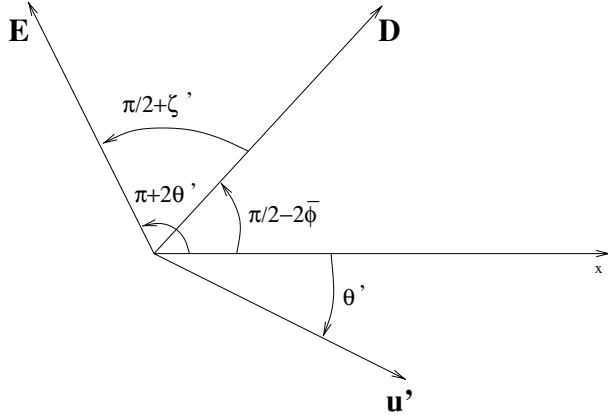


Fig. 1. Definition of the angle ζ' .

and they respectively characterize the perturbation anisotropy and the control flow deformation field. The scalar product between \vec{E} and \vec{D} that appears in eq. (1) is the so-called barotropic extraction term; it allows the perturbation to extract kinetic energy from the control flow. The other term in the rhs of (1) is the perturbation ageostrophic pressure work and it redistributes perturbation kinetic energy spatially. As the source of kinetic energy error growth in a barotropic context is due to $\vec{E} \cdot \vec{D}$, our analytical approach focuses on this term. We use the same notations as in RHK concerning the angles of \vec{u}' , \vec{E} and \vec{D} with the x-axis and the different definitions are summarized in Fig. 1. The deformation vector \vec{D} is decomposed into its modulus (usually called strain rate) and its angle as $\vec{D} = \bar{\sigma}(\cos(\pi/2 - 2\bar{\phi}), \sin(\pi/2 - 2\bar{\phi}))$. As the angle θ' denotes the angle of \vec{u}' with the x-axis, the \vec{E} vector can be written as $\vec{E} = K'(\cos(\pi + 2\theta'), \sin(\pi + 2\theta'))$ and its angle with the x-axis is $\pi + 2\theta'$. The previous definitions allows to define the angle

$$\zeta' \equiv 2\theta' + 2\bar{\phi}, \quad (3)$$

which is directly linked to the relative angle between \vec{E} and \vec{D} (Fig. 1) and the extraction term can thus be written as $\vec{E} \cdot \vec{D} = -K'\bar{\sigma} \sin \zeta'$. Eq. (1) can be written in a Lagrangian exponential form as

$$\frac{1}{K'} \frac{\bar{D}K'}{Dt} = -\bar{\sigma} \sin \zeta' + \frac{\vec{u}' \cdot \vec{\nabla} p'_1}{K'}. \quad (4)$$

In the previous equation, the unique variable depending on the perturbation structure that appears in the extraction term ($-\bar{\sigma} \sin \zeta'$) is the angle ζ' . It shows the crucial importance of ζ' to quantify at each time, the rate of perturbation kinetic energy extraction. As shown in the following paragraph, information concerning the time evolution of ζ' can be obtained analytically.

2.2. The Lagrangian orientation equation

From the linearized momentum equation, two equations can be derived; one is the perturbation kinetic energy eq. (1) and has been intensively used in the litterature to explore the control

flow/perturbation interaction, and the other is the orientation equation which has been analyzed in RHK. The orientation equation describes the dynamics of the perturbation velocity vector orientation and can be written in terms of the angle ζ' as shown in RHK. By projecting the perturbation ageostrophic pressure gradient on the orientation equation, the following useful approximate form for this equation can be deduced

$$\frac{\bar{D}\zeta'}{Dt} = \bar{\sigma}(r + \cos \zeta'). \quad (5)$$

The parameter r has been introduced by Lapeyre et al. (1999) for studying potential vorticity gradient dynamics. It depends solely on the control flow properties and is defined as

$$r \equiv \frac{\bar{\omega} + 2 \frac{\bar{D}\bar{\phi}}{Dt}}{\bar{\sigma}}, \quad (6)$$

where $\bar{\omega}$ is the relative vorticity, and $-2 \frac{\bar{D}\bar{\phi}}{Dt}$ is the rotation rate of the deformation vector \vec{D} along a Lagrangian path.

Let us briefly summarize the results of RHK concerning the fixed points of the orientation eq. (5). The fixed points of eq. (5) satisfy the property $\frac{\bar{D}\zeta'}{Dt} = 0$ and correspond to an angle ζ' that will not evolve rapidly along a Lagrangian path. There are two fixed points determined by $\zeta'_{\pm} \equiv \pm \arccos(-r)$, one (ζ'_{-}) imply kinetic energy extraction from the control flow to the perturbation whereas the other (ζ'_{+}) leads to loss of perturbation kinetic energy. It means that the perturbation structure is “in equilibrium” with the control flow deformation field. *RHK have shown that ζ'_{\pm} characterize the structure of the perturbations that have grown in the past.* More specifically, a Monte-Carlo method was used to prove that ζ' is statistically close to ζ'_{-} in regions of strong extraction ($\vec{E} \cdot \vec{D} > 0$, called hereafter the productive regions) and close to ζ'_{+} in regions where the conversion term is negative ($\vec{E} \cdot \vec{D} < 0$, called hereafter the destructive regions). Let us emphasize that such Lagrangian equilibrium orientations $\zeta' = \zeta'_{\pm}$ notably differ from the instantaneous optimal orientation $\zeta' = -\pi/2$ that is predicted by singular vectors approach for the case of spatially and temporally complex flows. In other terms, such orientations of the perturbation velocity vector differ from the dilatation and contraction axes of the control flow deformation field. In the following sections, we attempt to link the sustained phase of growth which characterizes perturbations that have grown in the past (in contrast with the transient growth of singular vectors) with the Lagrangian equilibrium determined by ζ'_{\pm} which leads to a sustained extraction (or sustained destruction) along a Lagrangian path.

3. Numerical model and methodology

3.1. Model and control flow

In the present study, we consider the classical oceanic problem of a wind-driven double gyre with a 6-layer quasigeostrophic code in a rectangular basin. The numerical code is presented in appendix C of RHK, or with more details in Schmitz and Holland (1986) and Barnier et al. (1991) and is not recalled

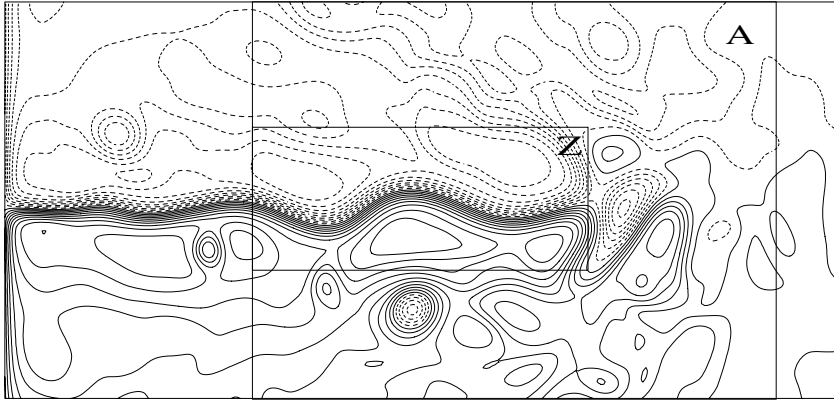


Fig 2. Control flow along the jet (streamfunction in the first layer). The notations A and Z correspond to two areas defined by the two boxes plotted in the figure.

here. As shown in Fig. 2, the flow is characterized by a strong jet that separates the southern anticyclonic gyre from the northern cyclonic one. The jet has meanders which can detach and form eddies that travel westward. In the next sections, we will study the initial error growth for this control flow and will focus on the limited area A covering the mid-basin and end part of the jet (see Fig. 2) because of its more varied and turbulent dynamical structures.

3.2. A new initialization method based on the perturbation velocity orientation

The principle of our method uses the recent results of RHK recalled in Section 2 of the present paper. The key idea is to initialize a perturbation whose structure corresponds to the most probable one of all the perturbations that have grown in the past, i.e. the structure determined at each grid point by the fixed points ζ_{\pm}^r of the Lagrangian orientation eq. (5). The aim is to obtain an algorithm for initializing a perturbation based on the sole knowledge of the control flow properties at initial time. The problem therefore amounts to building a perturbation streamfunction from the knowledge of the fixed points ζ_{\pm}^r . This will require several steps because (i) RHK theory does not analytically predict the location of the regions of production and destruction of perturbation kinetic energy in terms of the control flow properties, (ii) alignment dynamics provide a direction which is only defined modulo π , and lastly (iii) the perturbation velocity field has to be divergenceless. Thus, the first stage is to detect (step (i)) the location of regions of kinetic energy production and destruction in order to choose the right fixed point ζ_{\pm}^r at each grid point and to obtain the right value for ζ' ; the second step (ii) consists in invoking continuity properties to obtain the orientation of \vec{u}' . The last step (iii) is to obtain the perturbation streamfunction by knowing the orientation of \vec{u}' . In contrast with Section 2 based on mathematical evidences, the constraints leading to the determination of steps (i) to (iii) of the algorithm use heuristic results that are documented in appendix A. The three steps are detailed hereafter and it should be stressed that these additional stages of the initialization method are not independent and are actually necessary for obtaining the appropriate alignment of the perturbation.

3.2.1. (i) Determining regions of production and destruction of kinetic energy. The theory of Section 2 does not provide information on the location of the regions of production and destruction of kinetic energy. However, the statistical numerical results presented in Appendix A for perturbations that have grown in the past indicate that regions of production (and of destruction) tend to be located in specific regions of the control flow. In our simulations, the sign of the Lagrangian rate of change of the control flow kinetic energy $\frac{DK}{Dt} = -\vec{u} \cdot \vec{\nabla} \bar{p}_1$, or in other words the sign of the control flow acceleration, corresponds approximately in terms of spatial scales and location to the sign of the conversion rate $\vec{E} \cdot \vec{D}$. These results are consistent with those found by Snyder and Hamill (2003) and Snyder et al. (2003) in which it is shown that the perturbations that have grown in the past vary on a length scale comparable to that of the control flow. Following these heuristic results, the constraint imposed in our algorithm is the following

$$\zeta' \equiv \begin{cases} \zeta_{-}^r & \text{if } -\vec{u} \cdot \vec{\nabla} \bar{p}_1 > 0 \\ \zeta_{+}^r & \text{if } -\vec{u} \cdot \vec{\nabla} \bar{p}_1 < 0. \end{cases} \quad (7)$$

This statistical result can be physically interpreted as follows: along a Lagrangian path, in regions where the jet accelerates, i.e. where the control flow gains energy ($\frac{DK}{Dt} > 0$), it can release energy to the perturbation while in regions where the jet decelerates, it takes energy from the perturbation.

3.2.2. Step (ii): continuity properties. The constraint (7) do not define ζ' at each grid point as the fixed points ζ_{\pm}^r exist only in regions where $|r| < 1$. Which value of ζ' should be initialized in regions where fixed points do not exist? Our choice is to invoke the continuity of the preferred orientations in regions where $|r| > 1$. We therefore define $\zeta_{c\pm}^r$ the continuity prolongation of ζ_{\pm}^r as follows: $\zeta_{c\pm}^r \equiv \zeta_{\pm}^r = \pm \arccos(-r)$ if $|r| < 1$, $\zeta_{c\pm}^r \equiv \pm \pi$ if $r \geq 1$ and $\zeta_{c\pm}^r \equiv 0$ if $r \leq -1$. We remark that the values $\zeta_{c\pm}^r$ in regions where $|r| > 1$ correspond to values implying neither production and nor destruction. As ζ' is well defined and depends on the control flow structure as well as the angle $2\bar{\phi}$, we deduce from eq. (3) that $2\theta'$ depends on it too. This information gives only the direction of \vec{u}' as θ' is known modulo π ; θ' is either equal to $\frac{1}{2}(\zeta' - 2\bar{\phi})$ or to $\frac{1}{2}(\zeta' - 2\bar{\phi}) + \pi$. A continuity property at the top of the meanders can be invoked to remove the

orientation ambiguity and it leads to the following definition of the angle θ' of the perturbation (denoted θ^a)

$$\theta^a \equiv \begin{cases} \frac{1}{2}(\zeta_{c-}' - 2\bar{\phi}) & \text{if } -\vec{u} \cdot \vec{\nabla} \bar{p}_1 > 0 \\ \frac{1}{2}(\zeta_{c+}' - 2\bar{\phi}) + \pi & \text{if } -\vec{u} \cdot \vec{\nabla} \bar{p}_1 < 0. \end{cases} \quad (8)$$

3.2.3. Determination of perturbation streamfunction. The previous step of the algorithm defines exactly the angle θ' of the perturbation velocity vector \vec{u}' with the x-axis, from which we have to determine the perturbation streamfunction ψ' . No information is given on the modulus of \vec{u}' . Our choice is to initialize a perturbation whose kinetic energy is space-filling, i.e. with the same energetic weight at each grid point, $|\vec{u}'| = 1$. The reason is that, as no assimilation is taken into account, the uncertainties on the initial conditions are the same in all regions. Furthermore, this avoids one of the recurrent flaw of the total energy singular vectors which are excessively localized in one or two specific unstable regions.

We look for a streamfunction field such as $\vec{u}' = \vec{u}^a \equiv (\cos \theta^a, \sin \theta^a)$. It can be obtained by applying the following operation $\psi' = \Delta^{-1}(\partial_x \sin \theta^a - \partial_y \cos \theta^a)$ where Δ^{-1} designs the inverse of the horizontal Laplacian. However, there is no reason apriori that \vec{u}^a is a non divergent vector and that $-\partial_y \psi', \partial_x \psi'$ equals \vec{u}^a . By following the ideas of Jimenez et al. (1993), one method to minimize the divergent part of \vec{u}^a in dynamically relevant regions (i.e. regions where the jet is energetic in our case) is to resolve the following problem

$$\begin{aligned} \Delta \psi^{ai} &= \partial_x \sin \theta^a - \partial_y \cos \theta^a & \text{if } |\vec{u}| > |\vec{u}|_{\max}/p \\ \Delta \psi^{ai} &= 0 & \text{if } |\vec{u}| < |\vec{u}|_{\max}/p. \end{aligned} \quad (9)$$

The threshold chosen in our model is $p = 7$ (other values of $p \in [5, 10]$ have been also tested and lead to the same results). The streamfunction ψ^{ai} obtained by resolving the system (9) is called hereafter the Alignment-based Initialization mode and denoted AI. The use of the threshold allows us to initialise the streamfunction ψ^{ai} such as the angle of its velocity vector with the x-axis, θ^{ai} , is close to the angle we wanted to initialize θ^a (see Appendix A for the consistency of the algorithm). The other consequence of the threshold is to initialize a perturbation ψ^{ai} which is energetic where the control flow is itself energetic. This property is also a characteristic of the perturbations that have grown in the past as shown by Snyder and Hamill (2003) and Snyder et al. (2003).

3.3. Classical initialization methods

3.3.1. The Monte-Carlo method. Random perturbations are initialized by applying a white noise for the horizontal potential vorticity gradient in order to obtain a k^{-3} spectrum for the kinetic energy field. The exact algorithm is described in appendix D of RHK.

3.3.2. The singular vector method. The leading singular vectors used in the following sections are computed to maximize the amplification rate of a given norm within the area A for an optimization time of 10 days. The leading singular vector is the

first eigenvector of the matrix $S^{-1} \mathbf{R}^*(T) \mathbf{P}_A \mathbf{S} \mathbf{R}(T)$ (see for example, Buizza et al. (1993) or Farrell and Ioannou (1996)), where $\mathbf{R}(T)$ is the linear propagator for $T = 10$ days, $\mathbf{R}^*(T)$ is its adjoint for a given norm, \mathbf{S} is the matrix associated to the change of norm and \mathbf{P}_A represents the local projection operator on the area A. The local projection operator was introduced by Barkmeijer (1992) and Buizza and Palmer (1995). The norms used are total energy, potential enstrophy and potential palenstrophy (r.m.s of the potential vorticity gradient) and the corresponding singular vectors are respectively denoted SV_{te} , SV_{ens} and $\text{SV}_{\text{palens}}$.

3.3.3. Simulation of “bred modes”. In order to characterize the behavior of our AI mode, an ensemble of “simulated bred modes” have been initialized as follows: ten days before the initial time of the forecast ($t = -10$ days), random perturbations have been added to the control flow (the same random perturbations defined in Section 3.3.1) and perturbed runs of the fully non linear code lead to perturbations hereafter called “simulated bred modes” (by subtracting perturbed runs from the control run at $t = 0$). They therefore correspond to a single rescaling cycle (at $t = 0$). Let us remark that since no assimilation scheme has been considered, the control flow is not modified at the rescaling step.

4. Numerical results

4.1. Intercomparison of the different initial structures

Let us now intercompare the different initial structures obtained by the AI method and the singular vector method.

Let us first focus on the SVs spatial scales. It is a well-known property of the singular vector method that a norm associated with a smaller scale structures will correspond to a larger scale SV. This property is clearly exhibited in Fig. 3, as $\text{SV}_{\text{palens}}$ (Fig. 3c) has a larger scale than SV_{ens} (Fig. 3b) which itself has a larger scale than SV_{te} (Fig. 3a). The mathematical explanation is given by Moore and Mariano (1999), who also show more specifically why for very long optimization times the potential vorticity of $\text{SV}_{\text{palens}}$ (resp. SV_{ens}) equals the streamfunction of SV_{ens} (resp. SV_{te}).

The structure of $\psi_{\text{SV}}^{\text{te}}$ (Fig. 3a) is very localized in a specific region upstream of area A and its isolines clearly tilt against the shear. Strong similarities exist between the total energy SVs of our model and those computed by Moore and Mariano (1999) (see their Fig. 5). This configuration shows that both the angle and the modulus of SV_{te} are optimized to extract energy from the control flow in the specific region upstream of the area A. The structure of $\psi_{\text{SV}}^{\text{ens}}$ (Fig. 3b) is by contrast with $\psi_{\text{SV}}^{\text{te}}$, localized at the end part of the area A.

Figure 4 shows the structure of the AI mode streamfunction ψ^{ai} initialized from the control flow shown in Fig. 2. Its structure is quite different from the singular vectors structures, as its spatial scale is larger than SV_{te} and smaller than SV_{ens} . The mode in Fig. 4 is characterized by a succession of minima and maxima along the jet core, precisely in regions where the velocity of the

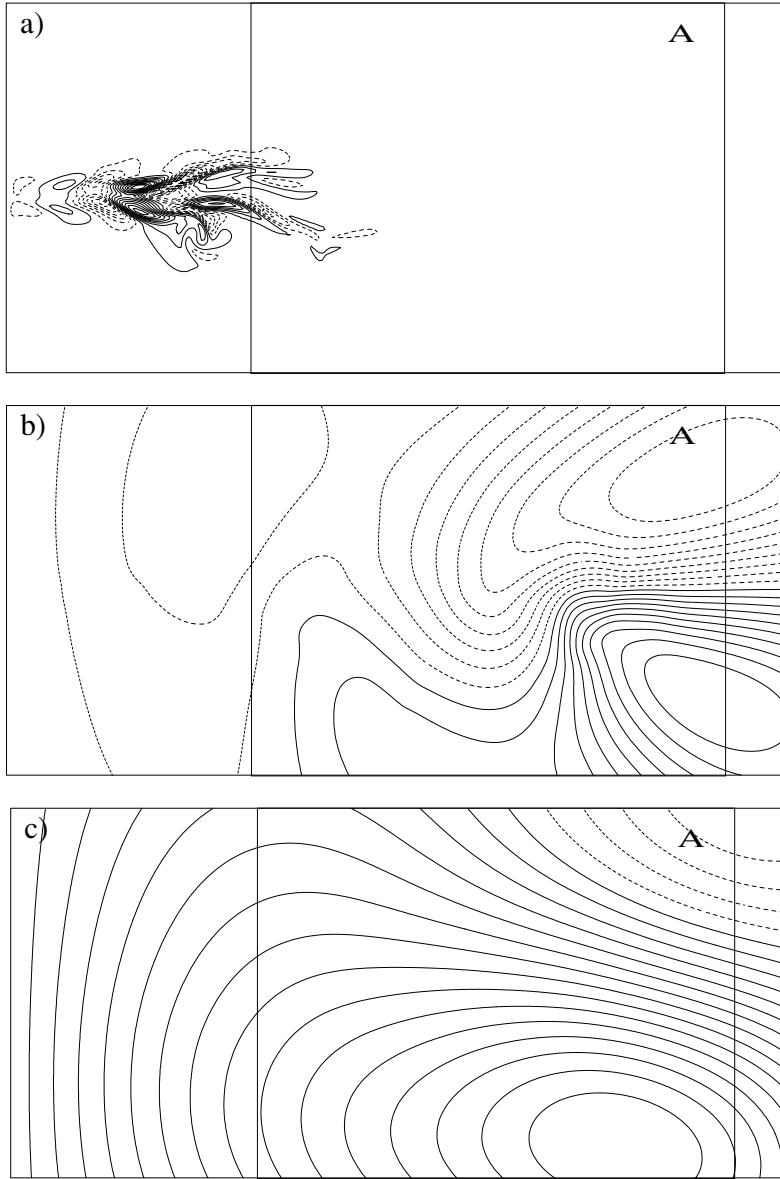


Fig 3. Zoom along the jet of the initial leading singular vectors streamfunctions for an optimization time of ten days for : (a) total energy (ψ_{SV}^{te}), (b) potential enstrophy (ψ_{SV}^{ens}) (c) and potential palenstrophy (ψ_{SV}^{palens}) norms.

jet is the strongest. This type of structure is quite different from the streamfunction of SV_{te} (Fig. 3) whose maxima and minima are localized on both sides of the jet core. Furthermore, as we have chosen $|\vec{u}'| = 1$ in our initialization algorithm, the AI mode is uniformly energetic in regions where the velocity of the control flow is strong.

4.2. Error growth

We will now intercompare the error fields within area A after 10 days obtained for three different methods: (1) an *ensemble mean* Monte-Carlo forecast computed with initially $N = 100$ random perturbations, (2) a *single* error forecast computed with the leading singular vector of three norms (SV_{te} , SV_{ens} and SV_{palens}), and (3) a *single* error forecast computed with our AI mode. All the perturbations are rescaled initially such that each one corresponds to an initial error of 10% in the kinetic energy

norm. They are added to the control flow to form different initial conditions of the model. Different trajectories of the non linear model are thus obtained; after 10 days, the difference between each perturbed run and the control run provides a single error forecast. Error forecasts are computed for the velocity error field. Single error forecasts, such as those obtained from the SV and AI methods, correspond to the value of $|\vec{u}'|$ the modulus of the perturbation velocity at each grid point, and are respectively noted $F_{SV}(u')$ and $F_{AI}(u')$, while the MC forecast is obtained by computing the root-mean-square of the perturbation velocities, $F_{MC}(u') \equiv \sqrt{\frac{1}{N} \sum_i u_i'^2}$. The MC error field is considered as the ground truth error field against which single error forecasts initialized with the SVs and AI methods will be intercompared.

Figure 5 shows the spatial localization of the different error forecasts. Let us look at the MC forecast (Fig. 5a), there is a strong growth of kinetic energy error along the jet, the center of

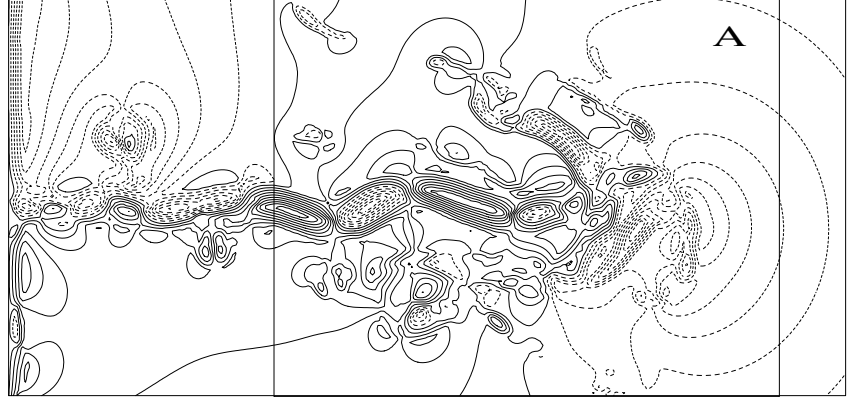


Fig 4. Streamfunction perturbation at $t = 0$ in the first layer for the AI mode ψ^{ai} .

the detached eddies and at the end part of the jet. The SV_{te} error forecast (Fig. 5b) does not capture globally the error growth deduced from the ensemble Monte-Carlo prediction, as it is characterized by a strong error growth at the beginning of area A, and not at all at the end part of the jet or around the eddies. This characteristic is due to the fact that SV_{te} is initially too much localized in a specific region upstream of the area A as mentioned previously (see Fig. 3a). For the SV_{ens} forecast (Fig. 5c), the error growth along the jet and around the main isolated eddy is visible but not as strong as for the MC forecast, while at the end part of the jet maxima of error growth are not always spatially correlated with those of the MC forecast. The $\text{SV}_{\text{palens}}$ forecast (Fig. 5d) captures very well the ensemble error field at the end part of the jet and at the center of the two isolated eddies but not along the jet. Finally, the AI error field (Fig. 5e) has the same maxima as those of the MC error field along the jet, and also at the main eddy center but the two fields do not correspond very well at the end part of the jet. Globally, the $\text{SV}_{\text{palens}}$ forecast (Fig. 5d) and the AI forecast (Fig. 5e) are thus much more representative of the MC forecast than the two other single forecasts. Let us now define the correlation of each single forecast j with the ensemble mean error field

$$C(j) = \frac{\iint_A F'_j(u') \cdot F'_{MC}(u')}{\sqrt{\iint_A F'^2_j(u') \cdot \iint_A F'^2_{MC}(u')}} \quad (10)$$

where the prime quantities are deviations from the spatial average over the domain A. The correlations of the SV_{te} (Fig. 5b), SV_{ens} (Fig. 5c), and $\text{SV}_{\text{palens}}$ (Fig. 5d) forecasts with the MC forecast (Fig. 5a) are respectively $C(\text{SV}_{\text{te}}) = 0.48$, $C(\text{SV}_{\text{ens}}) = 0.67$ and $C(\text{SV}_{\text{palens}}) = 0.75$. The correlation of the AI forecast (Fig. 5e) with the MC forecast is $C(\text{AI}) = 0.78$. So we conclude that for the present control flow, the AI forecast yields a similar score to the palenstrophy SV forecast and is much better than the total energy and enstrophy SV forecasts. However how do these modes perform when compared to a random perturbation initialization forecast? This can be assessed by the mean correlation of the MC ensemble defined by

$$\bar{C} = \frac{1}{N} \sum_i C(i), \quad (11)$$

with $N = 100$. At $T = 10$ days, for this control flow, $\bar{C} = 0.67$. On the one hand, $C_{\text{SV}_{\text{palens}}} > \bar{C}$, $C_{\text{AI}} > \bar{C}$ and on the other hand, $C_{\text{SV}_{\text{te}}} < \bar{C}$, $C_{\text{ens}} < \bar{C}$, so the $\text{SV}_{\text{palens}}$ forecast and the AI forecast give a better representation of error growth than a random one but the total energy and the enstrophy SV do not.

All the previous error forecasts are done for a specific control flow. Are the previous results robust if we change the control flow? To answer this question, the same error forecasts are computed for 20 different control flows. The correlations between the SVs forecasts and the MC forecast, $C(\text{SV}_{\text{ens}})$ and $C(\text{SV}_{\text{palens}})$, and between the AI forecast and the MC forecast $C(\text{AI})$, are shown for all these control flows in Fig. 6 as well as the mean correlation \bar{C} . As for each control flow, the correlation between the total energy singular vector and the MC forecast $C(\text{SV}_{\text{te}})$ is inferior to \bar{C} , the curve corresponding to $C(\text{SV}_{\text{te}})$ is not shown in Fig. 6. The total energy SV_{te} is not at all relevant and is typically less relevant than a random perturbation. This result could be quite surprising, but is due to the fact that SV_{te} is very localized initially whereas the random perturbations are more space-filling. For this specific diagnostic based on spatial localization of error growth, the leading total energy singular vector is not performant. It could be that secondary singular vectors for this norm will excite other unstable regions and a few energy SVs are needed to better represent the spatial distribution of the mean error field. However, since our AI mode is unique, we have compared it with the leading singular vector. The curves corresponding to $C(\text{SV}_{\text{ens}})$ (dashed line) and $C(\text{SV}_{\text{palens}})$ (dash-dotted line) are generally above the bold continuous curve corresponding to \bar{C} . SV_{ens} and $\text{SV}_{\text{palens}}$ are thus generally more relevant than a random perturbation, and the $\text{SV}_{\text{palens}}$ structure leads sometimes to strong correlations with the MC forecast. However, for some specific control flows, the two modes, SV_{ens} and $\text{SV}_{\text{palens}}$, yield bad scores. Indeed, the $C(\text{SV}_{\text{palens}})$ curve is under the \bar{C} curve for control flows numbered 5, 13 and 18, and $C(\text{SV}_{\text{ens}})$ is inferior to \bar{C} for control flows numbered 8, 13 and 15. This means that the two singular vectors for the potential enstrophy and palenstrophy norms are not systematically relevant for all control flows, even if they can give very good scores, sometimes better than the AI mode, for specific control flows. We have checked that singular vectors leading to bad scores are initially characterized by a too

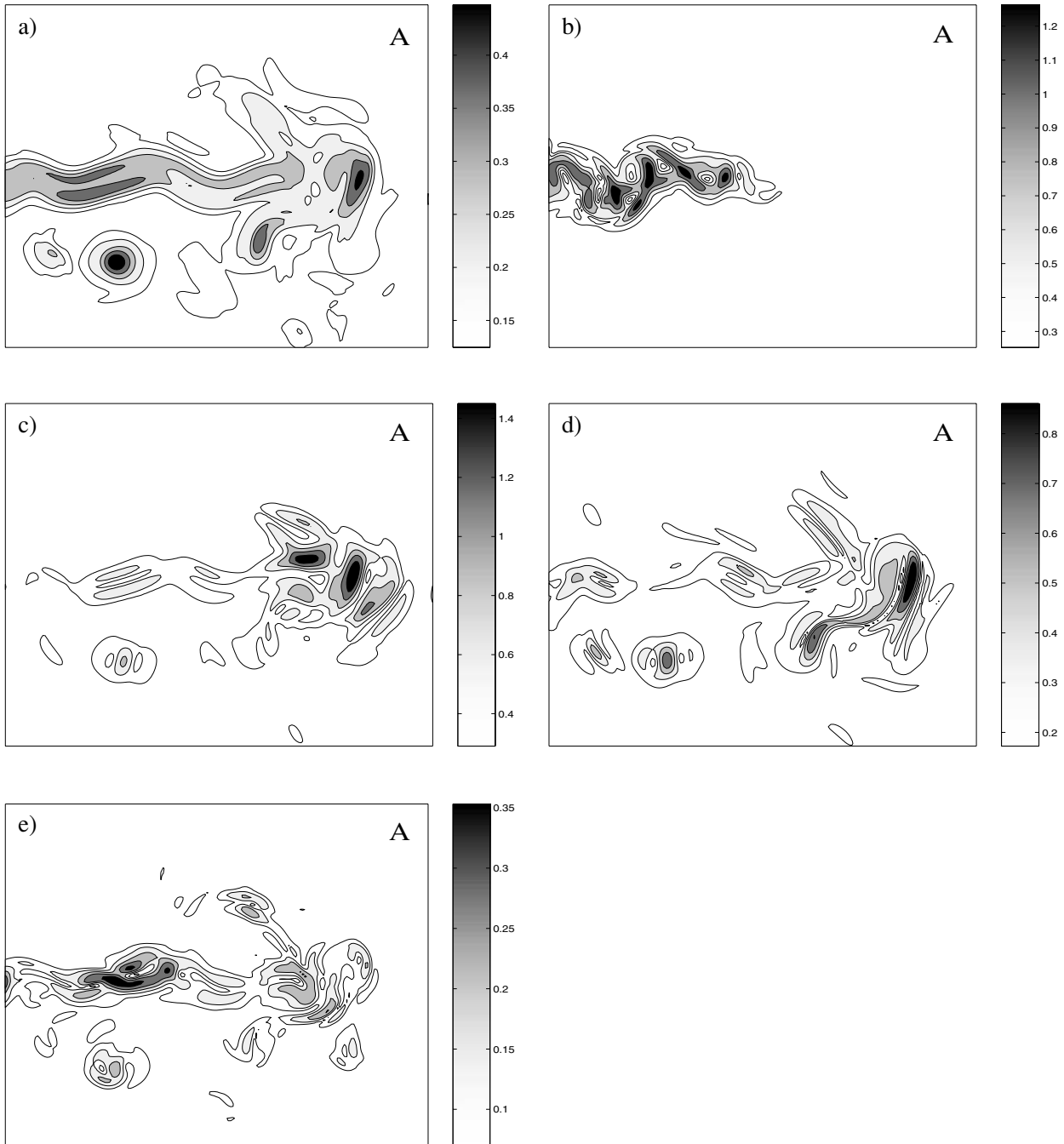


Fig 5. Spatial localization of kinetic energy error growth at $t = 10$ days in the first layer within the area A (see Fig. 2 for its definition); (a) ensemble Monte-Carlo forecast $F_{MC}(K')$, (b) total energy SV forecast $F_{SV}^{te}(K')$, (c) potential enstrophy SV forecast $F_{SV}^{ens}(K')$, (d) potential palenstrophy SV forecast $F_{SV}^{palens}(K')$ and (e) AI forecast $F_{AI}(K')$.

strong spatial localization in a specific region. We also note that the $C(AI)$ curve (thin continuous line) is systematically above \bar{C} for all control flows and that the difference $C(AI) - \bar{C}$ is of the order of the standard deviation of the random forecasts correlations with the mean correlation, which on average is 0.06. By contrast, the $C(SV_{palens})$ curve is sometimes below the \bar{C} curve as mentioned previously, even if $C(SV_{palens})$ is largely above $C(AI)$ for some cases. The AI forecast is systematically performant to

diagnose the ensemble mean error forecast which is not the case of SVs forecasts. This last result clearly proves the relevance of the AI method to localize systematically areas of strong error growth. Another important point to note concerns the practical interest of our AI approach; by contrast with the singular vectors initialization method, the numerical cost of the AI mode initialization method is negligible as it needs no additional run of the model.

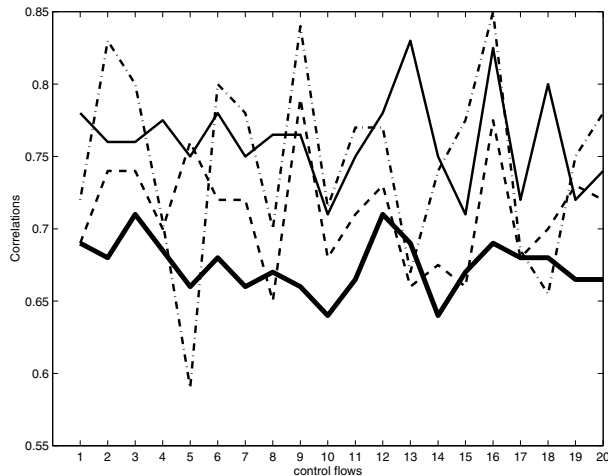


Fig 6. Correlations of different error forecasts with the average Monte-Carlo error forecast for 20 control flows; are represented the mean correlation of the MC ensemble \bar{C} (bold continuous line), two different SV forecasts correlations $C(SV_{ens})$ (dashed line) and $C(SV_{palens})$ (dash-dotted line) and the AI forecast correlation $C(AI)$ (thin continuous line).

4.3. Transient and sustainable growth

4.3.1. Time evolution of the different modes. Figure 7 shows the time evolution of three different perturbation streamfunctions corresponding to the AI mode (Figs. 7a and b), a “simulated bred mode” (Figs. 7c and d) and the palenstrophy SV (Figs. 7e and f) within the area A between $t = 0$ and $t = 10$ days. At final time, the three structures (Figs. 7b, d and f) are similar not only in terms of their spatial scales but also in terms of the structures themselves; along the jet, the three structures are characterized by a succession of negative and positive poles more or less energetic, and around the isolated eddies by two poles of opposite signs. This is not the case at initial time for which the palenstrophy SV differs completely from the two other fields as previously mentioned. By comparing now Fig. 7a with Fig. 7b, Fig. 7c with Fig. 7d and Fig. 7e with Fig. 7f, it is clear that the AI mode and the “simulated bred mode” structures undergo little modification of their spatial patterns with time, whereas the palenstrophy SV does. This change of spatial structures with time can be also noticed for energy and enstrophy singular vectors (not shown here), and is a classical result of the singular vectors structures. As for SV_{palens} , the enstrophy SV has a much larger spatial scale at initial time than at final time. Concerning the total energy SV, its initial horizontal structure strongly tilts against the horizontal shear (Fig. 3a), and at final time (not shown here), its streamfunction is characterized by a succession of positive and negative poles related to a succession of productive and destructive regions. The rapid time evolution of the energy and enstrophy SVs spatial structures are well known in the atmosphere since the works of Molteni et al. (1996) and Buizza and Palmer (1995) and are characteristics of rapid non modal transient growth. By contrast with SVs structures, the AI mode and the “simulated bred mode” are characterized by sustainable growth since the structures undergo

little changes with time. For example, the AI mode streamfunction has initially four poles along the jet (Fig. 7a) numbered from 1 to 4 which still exist at final time (Fig. 7b) with much larger amplitudes. The same result holds for the structure numbered 5 which is localized around the largest isolated eddy; the structure with two poles (a minimum and a maximum of streamfunction) at initial time is still recognizable at final time. Error growth along the eddy numbered 6 has disappeared at final time but corresponds to an eddy with initially less energy than the other one. As previously said, even if these structures do not correspond to an optimal configuration of growth (the poles along the jet are structured with both productive and destructive regions), they induce sustainable kinetic energy growth as in the case of “bred modes” structures.

In order to illustrate the distinction between transient and sustainable growth, the amplifications of the perturbation kinetic energy between $t = 0$ and $t = 10$ days for the AI mode, a “simulated bred mode”, an initially random perturbation and the SV_{palens} are shown in Fig. 8. The curves corresponding to the AI mode (continuous line) and the “simulated bred mode” (dashed line) remain quite close to each other, their slopes do not change much with time and even become constant and equal after about 4 days. This confirms our conclusions about Fig. 7 that the AI mode evolution is similar to the “simulated bred mode”’s one and that both characterize sustainable growth. Let us mention that the amplification curve of the “simulated bred mode” in Fig. 8 is not modified by choosing another perturbation among the bred mode ensemble and the results are therefore robust (the same remark being true for the initially random perturbation). By contrast with the AI mode and the “simulated bred vector”, the slopes of the amplification curves for the initially random perturbation (dotted-line) and the SV_{palens} (dash-dotted line) strongly change with time and therefore both are characterized by transient growth. The SV_{palens} (as well as the other singular vectors) has a stronger transient growth than the initially random perturbation which is not astonishing as by definition, the SV method characterizes explosive growth.

A detailed description of the transient phase of growth for initially random perturbations can be found in Snyder et al. (2003). Mechanisms by which the different Singular Vectors of different norms grow initially are developed in Snyder and Joly (1998) and Snyder (1999). The different behaviors of the singular vectors according to the chosen norm are recovered in our case. During their transient growth, the enstrophy and palenstrophy SVs have an initially large spatial scale and move toward a scale comparable to the control flow. Transient growth for these two norms are not related to a local extraction term. By contrast, the total energy SV (see Fig. 3) has an optimal configuration characterized by an initial strong tilt against the shear comparable to classical structures of total energy SVs (see Fig. 5 of Moore and Mariano, (1999) or Fig. 7 of Farrell (1990)). The non stationary character of the total energy SV structure can be interpreted in a Lagrangian point of view; the optimal configuration of kinetic energy extraction, i.e. when \vec{E} and \vec{D} are orthogonal

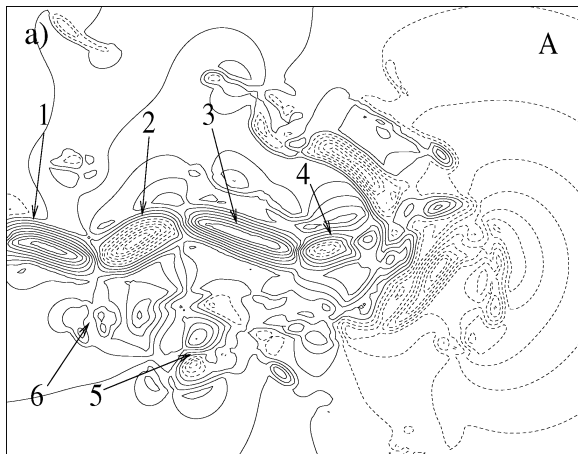
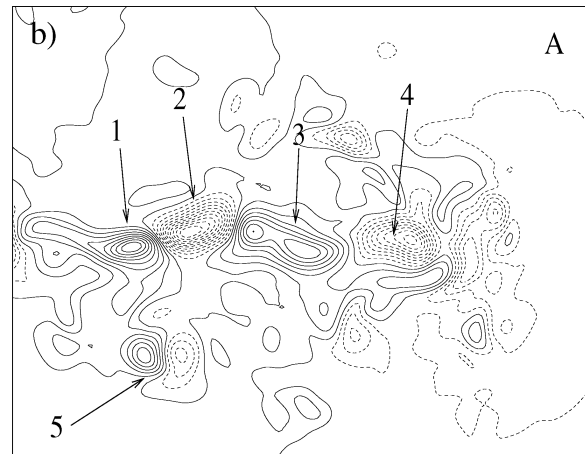
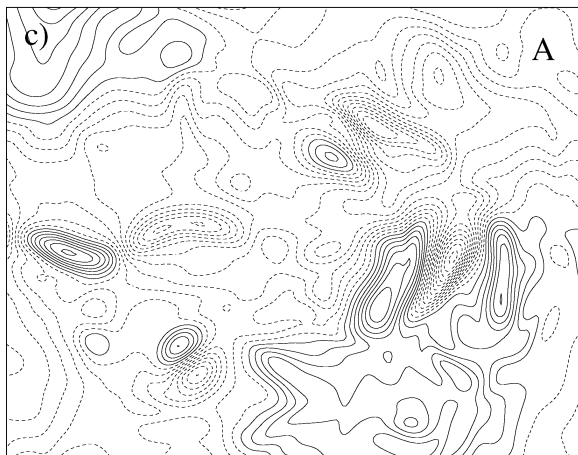
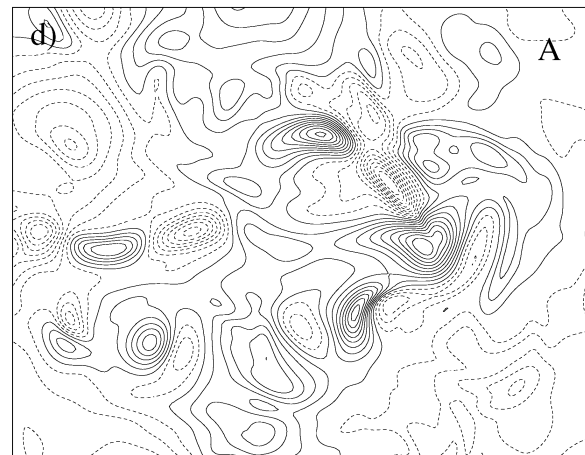
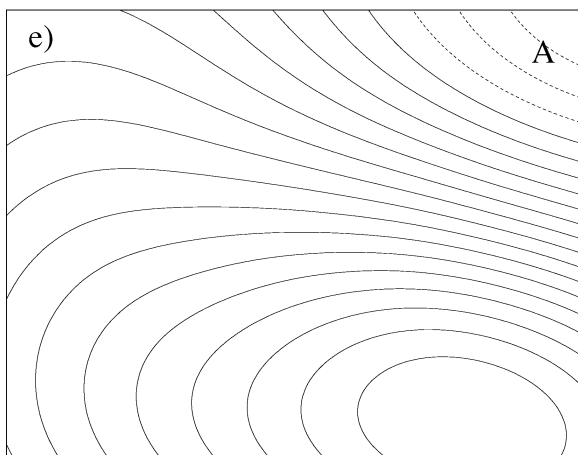
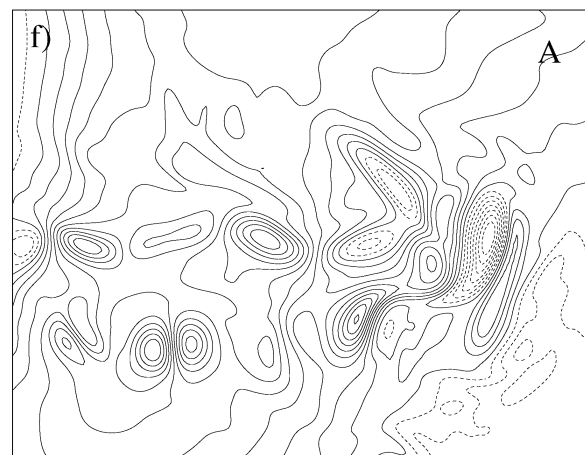
(a) AI, $t = 0$ (b) AI, $t = 10$ days(c) "bred mode", $t = 0$ (d) "bred mode", $t = 10$ days(e) SV_{palens} , $t = 0$ (f) SV_{palens} , $t = 10$ days

Fig 7. Time evolution of the streamfunction of different modes within the area A (see Fig. 2 for its definition) between $t = 0$ and $t = 10$ days; (a) and (b) correspond to the AI mode, (c) and (d) to a "simulated bred mode" and (e) and (f) to the potential palenstrophy singular vector.

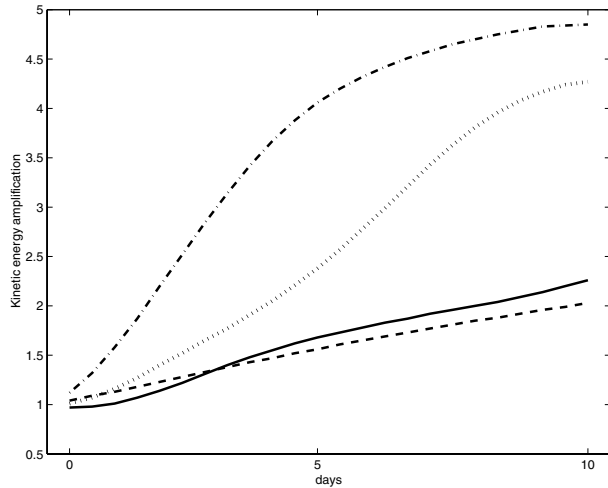


Fig 8. Amplifications of the perturbation kinetic energy $\frac{|\vec{u}'|}{|\vec{u}'|_0}$ within the whole basin between $t = 0$ and $t = 10$ days for the AI mode (continuous line), a “simulated bred mode” (dashed line), an initially random perturbation (dotted line) and the potential palenstrophy singular vector (dash-dotted line).

($\zeta' = -\pi/2$) do not correspond to the Lagrangian equilibrium $\zeta' = \zeta'_*$ in the general case where $r \neq 0$ and its angle will therefore evolve rapidly with time.

4.3.2. Principal component analysis at $t = 10$ days. The Principal component analysis is used in the present section as an other measure to prove the similarity between the “simulated bred modes” and the AI mode structures at the forecast time ($t = 10$ days). For each considered ensemble, the error covariance matrix is defined as follows

$$\text{COV}(k, l) = \frac{1}{N} \sum_i q'_i(k) q'_i(l), \quad k, l \in Z \quad (12)$$

where k and l correspond to two grid points belonging to the given area Z , N is the number of perturbations in the ensemble and q' is the perturbation potential vorticity. The first eigenvector of the error covariance matrix can be therefore considered as the most probable structure for the perturbations belonging to the studied ensemble. Two ensembles are considered in what follows, a Monte-Carlo and a “bred mode” ensemble. The error covariance matrix for each of these two ensembles is computed within a limited area Z localized around the jet core (see Fig. 2 for its location). This smaller domain Z has been chosen because the eigenvectors of the error covariance matrix computed in this specific region converge toward a given structure for $N = 100$ whereas we found no convergence when a principal component analysis is performed for the whole area A for example. The latter result appears to be due to the dynamical independence between the different parts of the flow, i.e. between the jet core, the isolated eddies, and the end part of the jet.

Figures 9a, b and c correspond respectively to the potential vorticities of the AI mode, of the first eigenvector of the error

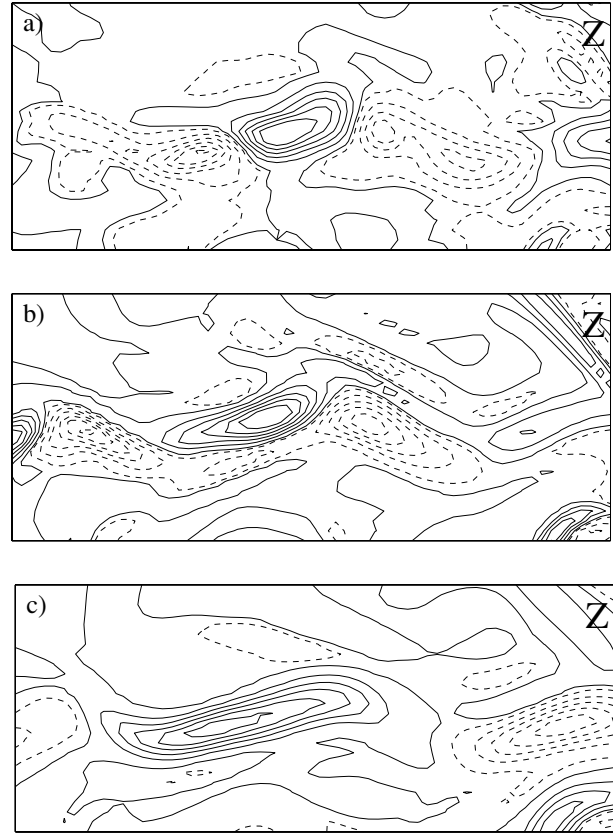


Fig 9. Potential vorticity q' at $t = 10$ days within the area Z located along the jet core (see Fig. 2 for its definition) for (a) the AI mode and (b) and (c) respectively the first eigenvectors of the error covariance matrix for the “bred mode” and Monte-Carlo ensembles.

covariance matrix for the “bred mode” ensemble (denoted as first BM eigenvector) and of the first eigenvector of the error covariance matrix for the Monte-Carlo ensemble (denoted as 1st MC eigenvector). For each ensemble, the first eigenvector explains 24% of the variance while the second one approximately 15%. The behavior of the two ensembles is therefore mainly captured by the first eigenvector. By comparing Fig. 9b with Fig. 9c, it is clear that the first MC eigenvector has a larger spatial scale than the first BM eigenvector (almost twice larger) as the latter is characterized by four poles of opposite signs along the jet whereas the first one by only two poles. It has been found (not shown here) that the scale and the structure of the first BM eigenvector (a succession of four poles) appears for the fourth MC eigenvector but the latter explains only 9% of the variance of the Monte-Carlo ensemble. There therefore exists a net difference between the BM and MC ensembles in terms of their spatial structure at forecast time. The scale of the AI mode (Fig. 9a) is comparable with that of the 1st BM eigenvector as it has also four poles of opposite signs along the jet. The projection of the AI mode on the 1st BM eigenvector is 0.33. Even if this value is not very strong, it has to be compared with

the projection of the AI mode on the 1st MC eigenvector which is approximately zero. From this principal component analysis, we conclude that the AI structure is closer to a “bred mode” structure than a Monte-Carlo structure at forecast time and this supports the conclusions of Section 4.3.1. We have checked that these results do not change by considering other control flows.

5. Discussion

A new perturbation initialization method to quantify error growth due to inaccuracies in the initial conditions of the model state has been developed and intercompared with classical numerical methods, the Monte-Carlo approach, the Bred Mode method and the Singular Vector method.

This new method is based on recent results on Lagrangian dynamics of the perturbation velocity vector in barotropic quasi-geostrophic flows. The essential ingredient comes from the Lagrangian barotropic extraction term $\vec{E} \cdot \vec{D}$ that allows a perturbation to extract energy from the basic flow, and more specifically from the angle (denoted $\pi/2 + \zeta'$) between the perturbation \vec{E} vector and the deformation vector of the control flow as its value determines the sign of the barotropic extraction term. The preferred values of the angle ζ' can be found by analyzing the Lagrangian formulation of the orientation equation of the perturbation velocity vector. It has been shown in a previous paper (RHK) that the most probable values of ζ' are composed of a couple (ζ'_- , ζ'_+) corresponding to the fixed points of the orientation equation, i.e. the values of ζ' for which the Lagrangian rate of change is zero. The proposed AI method consists in initializing a unique perturbation whose streamfunction isolines direction is given at each grid point by one of the two most probable directions ζ'_- and ζ'_+ . The choice between ζ'_- and ζ'_+ is given by the sign of the control flow Lagrangian acceleration which leads to a perturbation with a spatial scale comparable to that of the control flow. The perturbation can be therefore prescribed solely from the knowledge of the stirring properties of the control flow at the initial time of the forecast, a method which is conceptually and practically interesting (negligible numerical cost).

Let us now recall the results concerning the performance of the AI mode to diagnose areas of kinetic energy errors. The single AI forecast gives for all control flows a good spatial correlation (significantly better than a random initialization forecast) with the ensemble mean Monte-Carlo forecast. On average, the AI forecast yields the same correlation as the most relevant singular vectors forecast, the palenstrophy SV forecast. However, an examination of each case shows that the AI forecast is systematically relevant for all control flows whereas the palenstrophy SV forecast leads sometimes to very good scores and sometimes to very bad ones. Let us note finally that the AI forecast was found to be still relevant by comparing it with different types of MC methods in which random perturbations with small scales as well as large scales have been tested. Our results are not therefore dependent on the MC method chosen.

The second main conclusion of the paper is that the AI mode evolution provides a rationale of the perturbations that have grown in the past (i.e. before the initial time of the forecast) such as the “simulated bred vectors” used in the present paper. We have shown that the AI mode and the “simulated bred mode” have similar patterns and that these patterns do not change very much with time. At the forecast time, a principal component analysis around the jet core has shown that the AI mode structure is closer to a “simulated bred vector” structure than to an initially random perturbation one. Furthermore, by plotting the amplification of kinetic energy, it has been shown that the AI mode time evolution is characterized by a sustained phase of growth comparable to that of a “simulated bred mode”. The sustained phase of growth characteristic of the perturbations that have grown in the past can be therefore viewed in terms of a Lagrangian equilibrium of the perturbation velocity vector orientation in the strain axis. It should be contrasted with initially random perturbations and singular vectors behaviors which exhibit transient growth with a rapid time evolution of their spatial structures (cf. Snyder and Joly, 1998; Snyder et al., 2003).

As no assimilation procedure has been simulated in the present paper, the uncertainties in the initial conditions were considered to be the same in the whole domain. This is the reason why the choice $|\vec{u}'| = 1$ has been implemented in the AI mode initialization algorithm in the regions where the jet is energetic. By contrast, “simulated bred modes” are not everywhere energetic in these regions, and this is the main difference with the AI mode. An important point to note is that the robustness of our method has been also tested by modifying the angle but not the modulus of \vec{u}' . For example, we have initialized a perturbation with the optimal configuration $\zeta' = -\pi/2$ instead of the constraint $\zeta' = \zeta'_\pm$, i.e. a perturbation such as \vec{E} and \vec{D} are orthogonal at each grid point. The scores obtained with this perturbation in terms of spatial correlations were significantly inferior to \overline{C} for some control flows. It means that the performance of our AI mode is not due simply to the energy space-filling character of the method but rather to the values of the angle ζ' determined with the fixed points of the orientation equation. It has to be mentioned however that all the steps of the algorithm are necessary to initialize the right orientation for \vec{u}' . Finally, the AI method could be improved in particular for the heuristic step leading to the localization of the productive and destructive regions of kinetic energy. This step has been obtained by examining the time evolution of small amplitudes random perturbations and it would be better to replace it by a mathematical rationale.

A logical question that arises from the present study is: what would occur in a more practical situation when an assimilation procedure is taken into account and initial uncertainties are not the same everywhere. A feasible study that takes into account assimilation would be to modify the modulus of \vec{u}' according to the different uncertainties given by the error analysis. In this

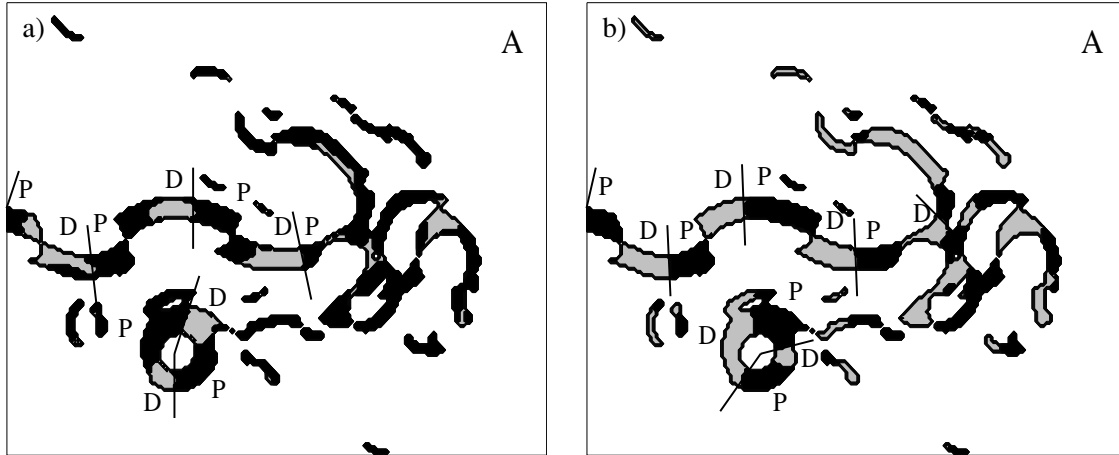


Fig 10. Spatial localization inside area A of the sign (a) of the ensemble mean barotropic extraction term $\langle \vec{E} \cdot \vec{D} \rangle$ for 100 independent realizations and (b) of the Lagrangian control flow acceleration $-\vec{u} \cdot \vec{\nabla} \bar{p}_1$. Regions in black (resp. in gray) correspond to regions where either $\langle \vec{E} \cdot \vec{D} \rangle$ or $-\vec{u} \cdot \vec{\nabla} \bar{p}_1$ is positive (resp. negative). Signs of the two quantities are shown only in regions where $|\vec{u}| > |\vec{u}|_{\max}/5$ and $|\bar{\omega}/\bar{\sigma}| < 1$. P and D denote regions where the quantity is respectively positive and negative.

context, an ensemble prediction could be initialized without any expensive numerical cost by giving different initial weights to the modulus of \vec{u}' and by keeping the same angle of \vec{u}' with the x-axis, i.e. θ^a , given by the fixed points of the orientation equation and obtained in Section 3.2.

6. Acknowledgments

The calculations reported here were done on the NEC SX-5 computer of the Institut du Développement et des Ressources en Informatique Scientifique, Orsay, France (project number 021217), and GR was supported by the Délégation Générale pour l'Armement, Paris, during this work.

7. Appendix: Details on the algorithm

7.1. Determining regions of production and destruction of kinetic energy

The determination of the regions of production and destruction of kinetic energy has been established numerically using a Monte-Carlo approach. 100 random perturbations of small amplitude have been initialized with the same Monte-Carlo method as in RHK and are added to the control flow shown in Fig. 2. The perturbations evolve for 10 days (linearly due to their initially small amplitude). Figure 10a shows the sign of the ensemble mean extraction term $\langle \vec{E} \cdot \vec{D} \rangle$ ($\langle \cdot \rangle$ denotes the ensemble mean computed with 100 independent realizations) after 10 days within the area A in regions where both the control flow is very energetic and its strain rate is stronger than its relative vorticity ($|\frac{\bar{\omega}}{\bar{\sigma}}| < 1$).

The last threshold corresponds approximately to regions where $|r| = |\frac{\bar{\omega} + 2\frac{D\bar{\phi}}{Dt}}{\bar{\sigma}}| < 1$ (i.e. regions where the fixed points exist) and has been preferred to the latter because of its more simple

spatial visualization. Black regions correspond to regions where the conversion rate is statistically positive, i.e. characterize productive regions whereas gray regions correspond to destructive regions. Perturbation structures along the jet core are characterized by a succession of productive and destructive regions (respectively noted by P and D) in which productive regions are localized downstream of the top of meanders whereas the destructive ones are upstream. Around the isolated eddy located in the south of the jet core, there are two productive regions and two destructive ones.

The sign of the extraction term previously diagnosed has been compared with different quantities depending on the control flow structure. The quantities to be tested are those involved in the control flow kinetic energy equation under its Lagrangian form, $\frac{D\bar{K}}{Dt} = -\vec{u} \cdot \vec{\nabla} \bar{p}_1$. The Lagrangian rate of change of the control flow kinetic energy (also called hereafter control flow acceleration), $-\vec{u} \cdot \vec{\nabla} \bar{p}_1$, was computed and its sign plotted in Fig. 10b. The quantity $-\vec{u} \cdot \vec{\nabla} \bar{p}_1$ is clearly characterized by an alternation of sign along the jet core, with a plus sign localized downstream of the top of each meander and a minus sign localized upstream. Even if the signs of $\langle \vec{E} \cdot \vec{D} \rangle$ (Fig. 10a) and $-\vec{u} \cdot \vec{\nabla} \bar{p}_1$ (Fig. 10b) are not entirely correlated along the jet, their properties of spatial localization with regard to the meanders are the same: the plus sign is downstream of the top of the meander whereas the minus sign is upstream. If we look at the isolated eddy in the left lower part of the domain A, two regions satisfy $-\vec{u} \cdot \vec{\nabla} \bar{p}_1 > 0$ and two others are such as $-\vec{u} \cdot \vec{\nabla} \bar{p}_1 < 0$. The sign of $-\vec{u} \cdot \vec{\nabla} \bar{p}_1$ change four times around the eddy as well as the sign of $\langle \vec{E} \cdot \vec{D} \rangle$ even if their signs are not spatially correlated in this specific region. The spatial distribution of the signs of the two quantities bears some resemblance, especially in terms of spatial scales. The knowledge of the sign of $-\vec{u} \cdot \vec{\nabla} \bar{p}_1$ will allow us to initialize the right fixed point at each grid point.

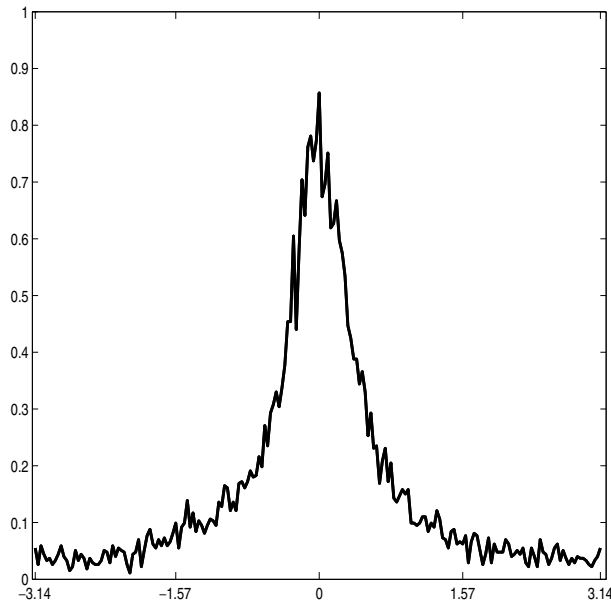


Fig 11. PDF of $\zeta^{ai} - \zeta^a$ in regions where $|\vec{u}| > |\vec{u}|_{\max}/7$ for the control flow shown in Fig. 2.

7.2. Check on the consistency of the algorithm

Let us now test if the direction of the isolines of ψ^{ai} (the stream-function which is effectively initialized) is actually equal or close to the direction we want to initialize, i.e. ζ^a . The angle ζ' deduced from the structure of ψ^{ai} is denoted ζ^{ai} , and it is compared with ζ^a by plotting in Fig. 11 the PDF of $\zeta^{ai} - \zeta^a = 2(\theta^{ai} - \theta^a)$ in regions where $|\vec{u}| > |\vec{u}|_{\max}/7$. The PDF is not a Dirac function, ζ^{ai} is not exactly equal to ζ^a , because the vector \vec{u}^a has a divergent part, as anticipated. However, the PDF has a strong peak for $\zeta^{ai} = \zeta^a$, meaning that ζ^{ai} is statistically close to ζ^a in regions of dynamical interest. The conclusion is that at most grid points, the structure determined by ζ^a is effectively initialized. We have therefore checked the consistency of our algorithm.

References

- Barkmeijer, J. 1992. Local error growth in a barotropic model. *Tellus* **44A**, 314–323.
- Barnier, B., Hua, B. L. and Leprovost, C. 1991. On the catalytic role of high baroclinic modes in eddy-driven large-scale circulations. *J. Phys. Oceanogr.* **21**, 976–997.
- Buizza, R. and Palmer, T. N. 1995. The singular-vector structure of the atmospheric general circulation. *J. Atmos. Sci.* **52**, 1434–1450.
- Buizza, R., Tribbia, J., Molteni, F. and Palmer, T. 1993. Computation of optimal unstable structures for a numerical weather prediction model. *Tellus* **45A**, 388–407.
- Farrell, B. F. 1990. Small error dynamics and the predictability of atmospheric flows. *J. Atmos. Sci.* **53**, 2409–2416.
- Farrell, B. F. and Ioannou, P. J. 1996. Generalized stability theory. Part I: autonomous operators. *J. Atmos. Sci.* **53**, 2025–2040.
- Frederiksen, J. S. 1997. Adjoint sensitivity and finite-time normal mode disturbances during blocking. *J. Atmos. Sci.* **54**, 1144–1165.
- Frederiksen, J. S. 2000. Singular vectors, finite-time normal modes, and error growth during blocking. *J. Atmos. Sci.* **57**, 312–333.
- Hamill, T. M., Snyder, C. and Morss, R. E. 2000. A comparison of probabilistic forecasts from bred, singular-vector, and perturbed observation ensembles. *Mon. Wea. Rev.* **128**, 1835–1851.
- Houtekamer, P. L. and Derome, J. 1995. Methods for ensemble prediction. *Mon. Wea. Rev.* **123**, 2181–2196.
- Houtekamer, P. L. and Coauthors. 1996. A system simulation approach to ensemble prediction. *Mon. Wea. Rev.* **124**, 1225–1242.
- Jimenez, J., Wray, A. A., Saffman, P. G. and Rogallo, R. S. 1993. The structure of intense vorticity in isotropic turbulence. *J. Fluid Mech.* **255**, 65–90.
- Lapeyre, G., Klein, P. and Hua, B. L. 1999. Does the traceur gradient vector align with the strain eigenvectors in 2D turbulence. *Phys. Fluids A* **11**, 3729–3737.
- Legras, B. and Vautard, R. 1996. A guide to Lyapunov vectors. *Proc. ECMWF Sem. on Predictability* Vol. 1, ECMWF, Reading United Kingdom, 143–156.
- Leith, C. E. 1974. Theoretical skill of Monte-Carlo forecasts. *Mon. Wea. Rev.* **102**, 409–418.
- Lorenz, E. N. 1965. A study of the predictability of a 28-variable atmospheric model. *Tellus* **17**, 321–333.
- Mak, M. and Cai, M. 1989. Local barotropic instability. *J. Atmos. Sci.* **46**, 3289–3311.
- Molteni, F., Buizza, R., Palmer, T. N. and Petroliagis, T. 1996. The ECMWF ensemble prediction system: Methodology and validation. *Quart. J. Roy. Meteor. Soc.* **122**, 73–120.
- Moore, A. M. and Mariano, A. J. 1999. The dynamics of error growth and predictability in a model of the Gulf Stream. Part I: Singular vector analysis. *J. Phys. Oceanogr.* **29**, 158–176.
- Moore, A. M. 1999. The dynamics of error growth and predictability in a model of the Gulf Stream. Part II: Ensemble prediction. *J. Phys. Oceanogr.* **29**, 762–778.
- Patil, D. J., Hunt, B. R., Kalnay, E., Yorke, J. A. and Ott, E. 2001. Local low dimensionality of atmospheric dynamics. *Phys. Rev. Lett.* **86**, 5878.
- Rivière, G., Hua, B. L. and Klein, P. 2003. Perturbation growth in terms of barotropic alignment properties. *Quart. J. Roy. Meteor. Soc.* **129**, 2613–2635.
- Schmitz, W. J. and Holland, W. R. 1986. Observed and modeled mesoscale variability near the Gulf Stream and Kuroshio Extension. *J. Geophys. Res.* **91**, 9624–9638.
- Snyder, C. 1999. Error growth in flows with finite-amplitude waves or coherent structures. *J. Atmos. Sci.* **56**, 500–506.
- Snyder, C. and Joly, A. 1998. Development of perturbations within a growing baroclinic wave. *Quart. J. Roy. Meteor. Soc.* **124**, 1961–1983.
- Snyder, C. and Hamill, T. M. 2003. Leading lyapunov vectors of a turbulent baroclinic jet in a quasigeostrophic model. *J. Atmos. Sci.* **60**, 683–688.
- Snyder, C., Hamill, T. M. and Trier, S. B. 2003. Linear evolution of error covariances in a quasigeostrophic model. *Mon. Weather Rev.* **131**, 189–205.

- Thompson, P. D. 1957. Uncertainty of initial state as a factor in the predictability of large-scale atmospheric flow patterns. *Tellus* **9**, 275–295.
- Toth, Z. and Kalnay, E. 1993. Ensemble forecasting at NMC: The generation of perturbations. *Bull. Amer. Meteor. Soc.* **74**, 2317–2330.
- Toth, Z. and Kalnay, E. 1997. Ensemble forecasting at NCEP and the breeding method. *Mon. Wea. Rev.* **125**, 3297–3319.
- Vannitsem, S. and Nicolis, C. 1997. Lyapunov vectors and error growth patterns in a T21L3 quasigeostrophic model. *J. Atmos. Sci.* **54**, 347–361.